6. Larson, R. L. & Chase, C. G. *Geol. Soc. Am. Bull.* **83,** 3627–3644 (1972).
7. Hilde, T. W. C., Isezaki, N. & Wageman, J. M. in *The Geophysics of the Pacific Ocean Basin and its Margin* Geophys. Mon. Ser. Vol. 19 (eds Sutton, G. H., Manghnani, M. & Moberly, R.) 205–226 (Am. Geophys. Union, Washington DC, 1976).
8. Sager, W. W., Handschumacher, D. W., Hilde, T. W. C. & Bracey, D. R. *Tectonophysics* **155,** 345–364 (1988).
9. Larson, R. L. *Geology* **19,** 547–550 (1991).
10. Harland, W. B. *et al. Geologic Time Scale* 140–165 (Cambridge Univ. Press, 1989).
11. Larson, R. L. & Moberly, R. *Init. Rep. DSDP* **32,** 159–192 (1975).
12. Sliter, W. V. & Brown, G. R. *Proc. ODP Sci. Res.* (in the press).
13. Toft, P. B. & Arkani-Hamed, J. *J. geophys. Res.* **97,** 4387–4406 (1992).
14. Plouff, D. *Geophysics* **41,** 727–741 (1976).
15. Harrison, C. G. A., Jarrard, R. D., Vacquier, V. & Larson, R. L. *Geophys. J. R. astr. Soc.* **42,** 859–882 (1975).
16. McNutt, M. K. *J. geophys. Res.* **91,** 3686–3700 (1986).
17. Larson, R. L. & Sager, W. W. *Proc. ODP Sci. Res.* **129,** 471–481 (1992).
18. Larson, R. L., Steiner, M. B., Erba, E. & Lancelot, Y. *Proc. ODP Sci. Res.* **129,** 615–631 (1992).
19. Gee, J., Staudigel, H. & Tauxe, L. *Nature* **342,** 170–173 (1989).
20. Sandwell, D. S. & MacKenzie, K. R. *J. geophys. Res.* **94,** 7403–7418 (1989).
21. Den, N. *et al. J. geophys. Res.* **74,** 1421–1421 (1969).
22. Gettrust, J. F., Furukawa, K. & Kroenke, L. W. *J. geophys. Res.* **85,** 5411–5415 (1980).
23. Clague, D. A. & Dalrymple, G. B. in *Volcanism in Hawaii* Vol. 1 (eds Decker, R. W., Wright, T. L. & Stauffer, P. L.) 5–54 (US Govt Printing Office, Washington DC, 1987).

Stability of orthorhombic $MgSiO_3$ perovskite in the Earth's lower mantle

Lars Stixrude* & R. E. Cohen†

* School of Earth and Atmospheric Sciences, Georgia Institute of Technology, Atlanta, Georgia 30332-0340, USA
† Geophysical Laboratory and Center for High Pressure Research, Carnegie Institution of Washington, 5251 Broad Branch Rd. NW, Washington DC 20015, USA

MAGNESIUM-rich silicate perovskite is thought to be the primary constituent of the Earth's lower mantle: experiments have shown[1] $MgSiO_3$ perovskite to be stable at lower-mantle pressures, and the elastic properties of perovskite-dominated assemblages agree well with seismological observations[2–4]. It has also been suggested[5–8] that the observed orthorhombic structure will undergo displacive phase transitions to higher-symmetry structures at lower-mantle conditions. The presence of such transitions would have important consequences for mantle convection[9], and could provide an explanation for some of the weak seismic discontinuities observed[10–12] in the lower mantle. However, the determination of the phase behaviour of $MgSiO_3$ perovskite at lower-mantle conditions has so far eluded both experimental and theoretical efforts. Here we report the results of electronic-structure calculations of the energetics of displacive phase transitions in $MgSiO_3$ perovskite, and demonstrate that the lower-symmetry orthorhombic phase should be highly favoured throughout the lower mantle. Our results are consistent with recent experiments[13] on $MgSiO_3$ perovskite encompassing the temperatures and pressures of the uppermost regions of the lower mantle.

We examined the orthorhombic, tetragonal and cubic phases of $MgSiO_3$ perovskite with the Linearized Augmented Plane Wave (LAPW) method[14], which yields essentially fully-converged solutions of the Schrödinger-like Kohn–Sham equations for all electrons (core and valence) within the Local Density Approximation[15] (LDA). The method makes no approximations to the shape of the charge density or the potential, nor to the nature of the bonding. The LDA, the only significant approximation in the calculations, typically yields agreement with observed volumes of a few per cent[14,16,17]. Thus, our results are expected to be the most accurate calculations of $MgSiO_3$ perovskite to date and to provide a firm theoretical basis for a discussion of the energetics of this mineral. The calculations are static, (0 K), so that structural energy differences represent energy barriers which must be overcome by high temperatures if phase transitions are to proceed.

The orthorhombic *Pbnm* structure is derived from the cubic polymorph (*Pm3m*) by coupled rotations of the SiO_6 octahedra ($a^-a^-c^+$ in Glazer's notation[18]) (Fig. 1). Two types of rotations are involved: (1), an in-phase rotation about the [001] pseudocubic axis ($00c^+$), is located at the *M*-point in the Brillouin zone (that is the rotation is modulated by a factor $\cos(-\mathbf{q}\cdot\mathbf{r})$ where $\mathbf{q}_M = (0.5, 0.5, 0)$ in units of $2\pi/a$, where a is the cubic lattice constant) and (2), an in-phase rotation about the [110] pseudocubic axis (a^-a^-0) consists of *R*-point rotations ($\mathbf{q}_R = (0.5, 0.5, 0.5)$). We have determined the energetics of the *M*-point (tetragonal $P4/mbm$ symmetry) and the *R*-point (tetragonal *Imma*) rotations individually throughout the pressure regime of the Earth's lower mantle (24–136 GPa). We have also calculated the total energy of the orthorhomic (*Pbnm*) structure over the same pressure range by homogeneously compressing the structure observed at ambient conditions[19]. Relative energies were converged to better than 2×10^{-4} Rydbergs (0.2 mRy) with respect to computational variables including the number of special **k**-points (6–20) and the number of basis functions (75–105 per atom).

Octahedral rotations at the *M* and *R* point lower the total energy with respect to the cubic polymorph (Fig. 2). The combination of these rotations in the orthorhombic structure produces the lowest-energy structure. This shows that the calculations correctly predict that the orthorhombic structure is the stable phase at low temperatures. The energy difference between low- and high-symmetry structures increases with compression, in accordance with the typically positive Clapeyron slope of orthorhombic to tetragonal and tetragonal to cubic displacive phase transitions in other perovskite compounds[5]. These general features are consistent with the results of *ab initio* ionic models[8,20,21], although in the LAPW calculations, the total energy depends much more strongly on the octahedral rotations due to covalent forces not included in the ionic calculations.

Our results are in excellent agreement with the experimentally determined equation of state[1,22] (Fig. 3). The computed curve implies that the material is slightly denser and stiffer (larger bulk modulus) than experiment, consistent with the lack of 300 K thermal pressure in the calculations. Similar levels of agreement were found in LAPW calculations of MgO periclase and SiO_2 stishovite[16,17]. The good agreement indicates that inhomogeneous compression mechanisms, such as pressure-induced lattice distortion (small amounts of which are detected experimentally[22]), and octahedral rotation and deformation, are not important in this mineral. The equations of state of all four polymorphs are nearly parallel (similar bulk moduli at a given volume) indicating similar compression mechanisms in all four

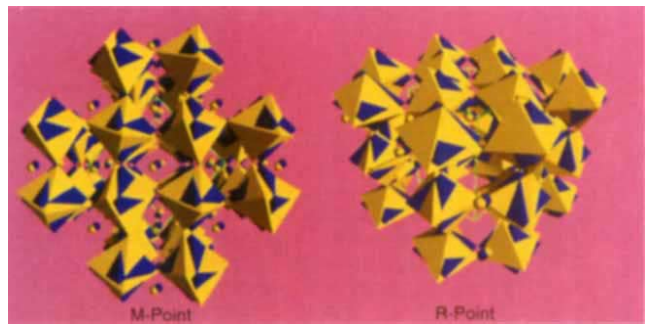

FIG. 1 Structure of $MgSiO_3$ perovskite viewed along the *M*-point rotation axis (left) and showing the *R*-point rotation axis (right). The orthorhombic *Pbnm* structure (yellow octahedra) is superimposed on the cubic *Pm3m* structure (purple octahedra) to show the octahedral rotations. The green lines define the orthorhombic unit cell and the small spheres are the Mg atoms.

structures. This also points toward a minor role for inhomogeneous compression mechanisms because these are unavailable to the cubic structure. As expected, volumes of the tetragonal phases are slightly larger (3%) than orthorhombic volumes at the same pressure, and the cubic volumes are 5% larger.

We address the possibility of displacive phase transitions in $MgSiO_3$ perovskite by comparing structural energy differences with plausible temperatures in the lower mantle (~2,000–3,000 K). The total energies of the tetragonal and cubic polymorphs relative to the orthorhombic structure are shown as a function of pressure in Fig. 4. Comparison with a range of estimated geotherms and the melting curve of $Mg_{0.9}Fe_{0.1}SiO_3$ perovskite shows that the energy differences are 2–6 times larger than the thermal energy available in the lower mantle, making displacive phase transitions unlikely. Even the possibility of anion sub-lattice melting in the high symmetry phases[42] can lower their free energies relative to the orthorhombic structure by no more than the available thermal energy. Coupling of octahedral rotations with lattice strain, which has been neglected in our calculations, will affect the relative energies of these structures somewhat. Relaxation of the structure, however, would make the lowest-symmetry polymorph (orthorhombic) even more favourable energetically. In any case, the effect of strain-rotation coupling appears to be small relative to the calculated energy differences between structures: calculations show that the energy of the orthorhombic structure differs from that of the corresponding unstrained lattice ($a=b=c/\sqrt{2}$) by only 200 K per octahedron. Recent pseudo-potential calculations in which the energy of the *Pbnm* structure was minimized with respect to all its structural parameters find energies (relative to the cubic structure) that are within 20% of our results[23].

The LAPW results show that the orthorhombic *Pbnm* structure is highly favourable energetically. Although other structures exist which may be produced by octahedral rotations[24], the very strong dependence of the lattice energy on the individual *M*- and *R*-point rotations make any displacive phase transition in

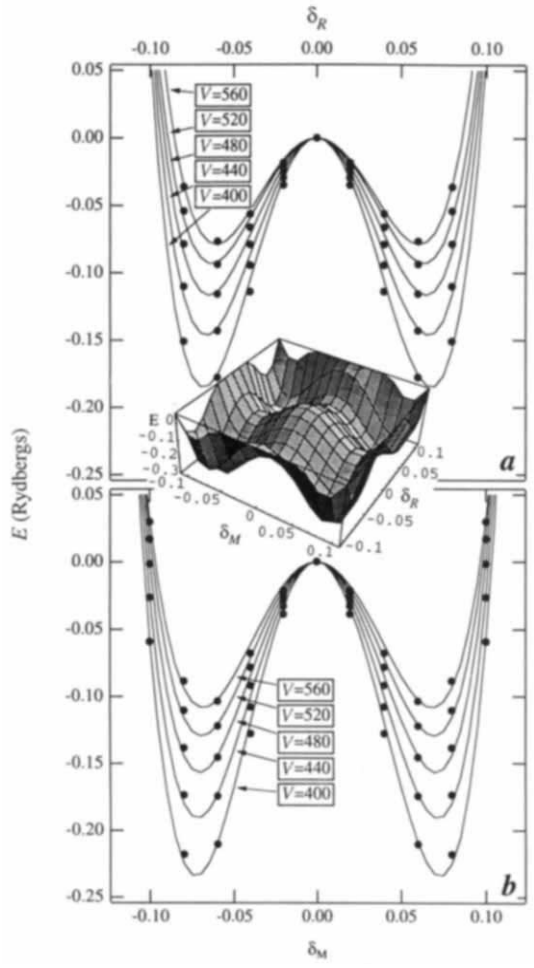

FIG. 2 Energetics of octahedral rotations. Calculated (LAPW) total energies (ten atoms) relative to the cubic structure are plotted (points) as a function of the *R*-point (*a*) and *M*-point (*b*) rotation angle, represented by the fractional change in the oxygen coordinate (δ_R and δ_M respectively), for five different volumes. Orthorhombic results ($\delta_M=0.0766$, $\delta_R=0.0912$) are shown in Fig. 3. We represented the *M*-point, *R*-point and orthorhombic results by a low-order Landau expansion of the energy relative to the cubic structure: $E=a\delta_M^2+b\delta_M^4+c\delta_R^2+d\delta_R^4+e\delta_M^2\delta_R^2$ where the values of the coefficients can be expressed in Rydbergs as $a=-46.25(V_0/V)^{1.90}$, $b=4943(V_0/V)^{1.50}$, $c=-39.89(V_0/V)^{2.07}$, $d=5177(V_0/V)^{1.52}$, $e=-2500$, where V is the unit cell volume (ten atoms) and $V_0=560$ bohr^3. The inset shows the energy surface at $V=480$ bohr^3, The orthorhombic structure lies in the absolute minima, the tetragonal structures on the local minima (saddle points) and the cubic structure at the local maximum in the centre.

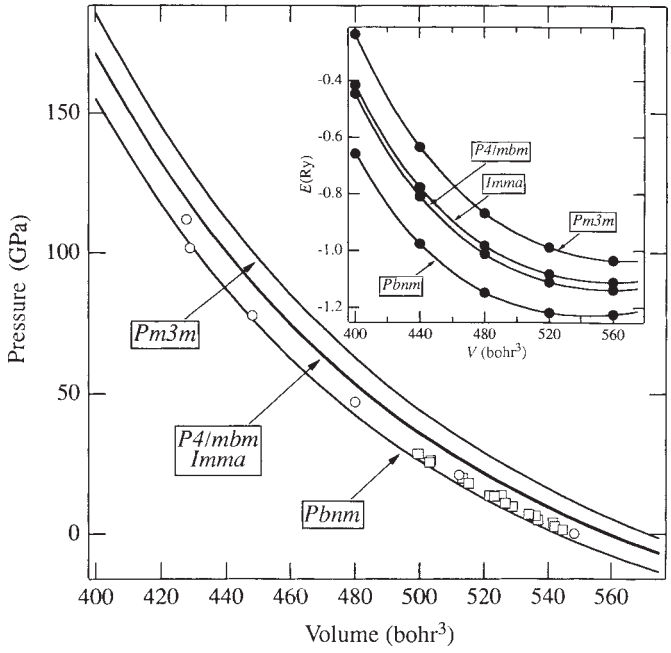

FIG. 3 Predicted equations of state of orthorhombic (*Pbnm*), tetragonal (*Imma* and *P4/mbm*) and cubic (*Pm3m*) phases compared with room temperature experimental data on the orthorhombic phase (circles[1]; squares[22]). Predicted *P4/mbm* and *Imma* equations of state are essentially coincident on this scale. The inset shows the calculated energies (ten atoms) of the four structures (*E*, in Rydbergs), as a function of *V* (in bohr^3). Results for the cubic phase are essentially identical to those of ref. 32. Tetragonal points are those of the minimum energy octahedral rotation. Equations of state were derived by fitting the *E* against *V* curves to a Birch–Murnaghan form[33]. The predicted equation of state parameters of the orthorhombic structure are: zero pressure volume, $V_0=24.2$ cm^3 mol^{-1}; zero pressure bulk modulus, $K_0=266$ GPa; and pressure derivative of the bulk modulus at zero pressure, $K_0'=4.2$. These compare favourably with experimental values[22] $V_0=24.46$ cm^3 mol^{-1}, $K_0=261$ GPa, $K_0'=4$. Differences in V_0 and K_0 between theory and experiment are consistent with the lack of 300 K and zero-point thermal pressure in the calculations. Experimental volumes have been corrected for iron content[34].

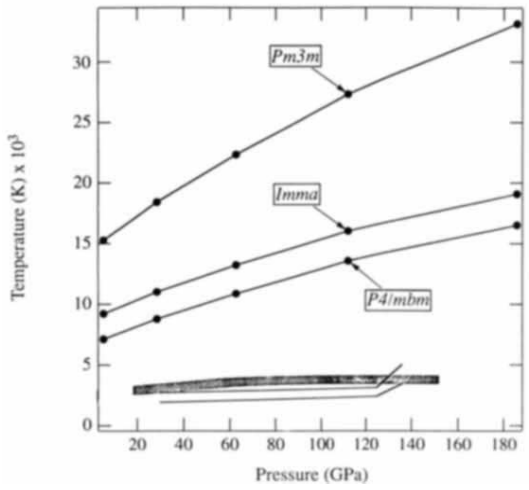

FIG. 4 The calculated (LAPW) total energy of tetragonal (*Imma*, *P4/mbm*) and cubic (*Pm3m*) structures relative to the orthorhombic structure, expressed in terms of temperature per octahedron (five atoms) and shown as a function of pressure. Also shown are two lower mantle geotherms which encompass most previous estimates[35,36] (lines) and the melting curve of $(Mg_{0.9},Fe_{0.1})SiO_3$ perovskite (broad shaded line). The melting curve represents an upper bound to lower mantle temperatures because this region is known to be almost completely solid[37] (the consequences of the intersection of the uppermost geotherm and the melting curve near the bottom of the lower mantle have been discussed in ref. 38). The melting curve is that calculated in ref. 39 and is consistent with available data[40,41].

perovskite unlikely in the Earth. Also unlikely to affect the stability of orthorhombic perovskite are the unknown effects of Fe substitution (which replaces up to 10% of Mg) or oxygen defects (which are commonly observed in other perovskites but not yet detected in $(Mg,Fe)SiO_3$). Our results do not support predictions of a high-temperature phase transition below melting[8] nor the interpretation of thermal expansion data[6], observed twinning patterns in quenched specimens[5,7] nor pressure-induced changes in Raman intensities[25]. The thermal expansion data of ref. 6 may be biased by texturing effects[24] and the observed volume discontinuity (interpreted as a phase transition) has not been reproducible. The twinning observations are difficult to interpret uniquely and patterns similar to those observed are seen in other minerals which have not undergone phase transitions during quench[26]. Interpretation of Raman intensities in terms of a room-temperature phase transition is not supported by X-ray determinations of the high pressure crystal structure[1]. Recent X-ray diffraction results[13] find that the orthorhombic structure persists to at least 2,000 K at 36 GPa, corresponding to the uppermost lower mantle (950 km depth), in excellent agreement with our results. These data require the orthorhombic phase to be stable throughout most of the lower mantle.

The wide stability field of orthorhombic Mg-rich silicate perovskite predicted here supports the view that this mineral is the primary constituent of the Earth's lower mantle and that its structure remains *Pbnm*[2,4]. Speculation that the uppermost lower mantle is weakened and viscously decoupled from the upper mantle because of grain-size effects associated with a displacive transition in perovskite[9] are not supported. In view of our results a mechanism other than a phase transition in Mg-rich silicate perovskite must be sought to explain seismic discontinuities within the lower mantle at 710, 900, 1,200 and 2,640 km depth[10-12]. Possible mechanisms for producing these features include the garnet to perovskite transition[10], phase transitions in other lower-mantle minerals, possibly stishovite[27], rapid changes in deformation mechanism[28], and a rapid change in bulk chemical composition with depth. The irregular and intermittent upper boundary of the D″ layer near 2,640 km depth[12] may be a compositional boundary caused by widespread chemical reactions between mantle and core[29]. If the 710, 900 and 1,200 km discontinuities are shown to be equally patchy, they may also have a compositional origin, perhaps related to subducting slabs that have either penetrated into the lower mantle[10], or deflected the compositional boundary[4] between upper and lower mantles by 50–500 km.

Theory will play an important role in deciding between models of lower-mantle seismic discontinuities and in further tests of the perovskite-rich lower mantle hypothesis. The LAPW calculations provide a data base which can be used to determine high temperature physical properties of the phases that make up the deep Earth. The total energies and band structure can be used to constrain potential[30] and/or tight-binding[31] models that allow calculation of thermodynamic, elastic, transport and anelastic properties at the pressures and temperatures of the deep interior. Predictions of the shear wave velocity, for example, as yet unknown for lower-mantle minerals at high pressures, will test our picture of lower-mantle composition, constructed essentially independently of this important seismic observable. □

Received 12 March; accepted 14 June 1993.

1. Knittle, E. & Jeanloz, R. *Science* **235,** 668–670 (1987).
2. Jeanloz, R. & Knittle, E. *Phil. Trans. R. Soc.* A **328,** 377–389 (1989).
3. Bukowinski, M. S. T. & Wolf, G. H. *J. geophys. Res.* **95,** 12583–12593 (1990).
4. Stixrude, L., Hemley, R. J., Fei, Y. & Mao, H. K. *Science* **257,** 1099–1101 (1992).
5. Wang, Y., Guyot, F. & Liebermann, R. C. *J. geophys. Res.* **97,** 12327–12347 (1992).
6. Wang, Y. *et al. Science* **251,** 410–413 (1991).
7. Wang, Y., Guyot, F., Yeganeh-Haeri, A. & Liebermann, R. C. *Science* **248,** 468–471 (1990).
8. Wolf, G. H. & Bukowinski, M. S. T. *Geophys. Res. Lett.* **12,** 809–812 (1985).
9. Karato, S. & Li, P. *Science* **255,** 1238–1249 (1992).
10. Revenaugh, J. & Jordan, T. H. *J. geophys. Res.* **96,** 19763–19780 (1991).
11. Wicks, C. W. & Richards, M. A. *EOS* **73,** 522–523 (1992).
12. Lay, T. *EOS* **70,** 54–55, 58–59 (1989).
13. Funamori, N. & Yagi, T. *Geophys. Res. Lett.* **20,** 387–390 (1993).
14. Wei, S. H. & Krakauer, H. *Phys. Rev. Lett.* **55,** 1200–1203 (1985).
15. Hedin, L. & Lundqvist, B. I. *J. Phys.* C**4,** 2064–2083 (1971).
16. Mehl, M. J., Cohen, R. E. & Krakauer, H. *J. geophys. Res.* **93,** 8009–8022 (1988).
17. Cohen, R. E. *Am. Miner.* **76,** 733–742 (1991).
18. Glazer, A. M. *Acta Crystallogr.* B **28,** 3384–3391 (1972).
19. Horiuchi, H., Ito, E. & Weidner, D. J. *Am. Miner.* **72,** 357–360 (1987).
20. Hemley, R. J., Jackson, M. D. & Gordon, R. G. *Phys. Chem. Miner.* **14,** 2–12 (1987).
21. Cohen, R. E. *Geophys. Res. Lett.* **14,** 1053–1056 (1987).
22. Mao, H. K. *et al. J. geophys. Res.* **96,** 8069–8079 (1991).
23. Wentzcovitch, R. M., Martins, J. L. & Price, G. D. *Phys. Rev. Lett.* **70,** 3947–3950 (1993).
24. Hemley, R. J. & Cohen, R. E. *A. Rev. Earth planet. Sci.* **20,** 553–600 (1992).
25. Chopelas, A. & Boehler, R. in *High Pressure Research: Applications to Earth and Planetary Sciences* (eds Syono, Y. & Manghnani, M. H.) 101–108 (Am. Geophys. Union, Washington DC & Terra Scientific, Tokyo, 1992).
26. Smith, J. V. & Brown, W. L. *Feldspar Minerals* Vol. 1 Ch. 18 (Springer, Berlin, 1988).
27. Cohen, R. E. in *High Pressure Research: Applications to Earth and Planetary Sciences* (eds Syono, Y. & Manghnani, M. H.) 425–432 (Am. Geophys. Union, Washington DC & Terra Scientific, Tokyo, 1992).
28. Karato, S. *Geophys. Res. Lett.* **19,** 2255–2258 (1992).
29. Knittle, E. & Jeanloz, R. *Geophys. Res. Lett.* **16,** 609–612 (1989).
30. Gong, Z. & Cohen, R. E. *Ferroelectrics* **136,** 113–124 (1992).
31. Khan, F. S. & Broughton, J. Q. *Phys. Rev.* B**39,** 3688–3700 (1989).
32. Cohen, R. E., Boyer, L. L., Mehl, M. J., Pickett, W. E. & Krakauer, H. in *Perovskite: A Structure of Great Interest to Geophysics and Materials Science* (eds Navrotsky, A. & Weidner, D. J.) 55–66 (Am. geophys. Union, Washington DC, 1991).
33. Birch, F. *J. Geophys. Res.* **91,** 4949–4954 (1986).
34. Jeanloz, R. & Thompson, A. B. *Rev. Geophys. Space Phys.* **21,** 51–74 (1983).
35. Jeanloz, R. & Morris, S. *A. Rev. Earth planet. Sci.* **14,** 377–415 (1986).

36. Jeanloz, R. *A. Rev. Earth Planet. Sci.* **18,** 357–386 (1990).
37. Lee, R. C. & Johnson, L. R. *Geophys. J. R. Astr. Soc.* **77,** 667–681 (1984).
38. Stixrude, L. & Bukowinski, M. S. T. *Geophys. Res. Lett.* **19,** 1057–1060 (1992).
39. Stixrude, L. & Bukowinski, M. S. T. *J. geophys. Res.* **95,** 19311–19325 (1990).
40. Heinz, D. L. & Jeanloz, R. *J. geophys. Res.* **92,** 11437–11444 (1987).
41. Knittle, E. & Jeanloz, R. *Geophys. Res. Lett.* **16,** 421–424 (1989).
42. Matsui, M. & Price, G. D. *Nature* **351,** 735–737 (1991).

ACKNOWLEDGEMENTS. We thank C. Lithgow-Bertelloni, R. J. Hemley and P. Shearer for discussions and L. Finger for assistance in preparing Fig. 1. Computations were performed on the Cray YMP and Cray 2 at the National Center for Supercomputing Applications. This work was supported by NSF.

Evidence of a feedback mechanism limiting plant response to elevated carbon dioxide

S. Díaz*, J. P. Grime, J. Harris† & E. McPherson†

Unit of Comparative Plant Ecology (NERC), Department of Animal and Plant Sciences, The University, Sheffield S10 2TN, UK
* Facultad de Ciencias Exactas, Físicas y Naturales, Universidad Nacional de Córdoba, C. Correo 495, 5000 Córdoba, Argentina
† Environment & Industry Research Unit, University of East London, Romford Road, London E15 4LZ, UK

In short-term experiments under productive laboratory conditions, native herbaceous plants differ widely in their potential to achieve higher yields at elevated concentrations of atmospheric carbon dioxide[1–8]. The most responsive species appear to be large fast-growing perennials of recently disturbed fertile soils[7,8]. These types of plants are currently increasing in abundance[9] but it is not known whether this is an effect of rising carbon dioxide or is due to other factors. Doubts concerning the potential of natural vegetation for sustained response to rising carbon dioxide have arisen from experiments on infertile soils, where the stimulus to growth was curtailed by mineral nutrient limitations[2,3,10]. Here we present evidence that mineral nutrient constraints on the fertilizer effect of elevated carbon dioxide can also occur on fertile soil and in the earliest stages of secondary succession. Our data indicate that there may be a feedback mechanism in which elevated carbon dioxide causes an increase in substrate release into the rhizosphere by non-mycorrhizal plants, leading to mineral nutrient sequestration by the expanded microflora and a consequent nutritional limitation on plant growth.

Effects of doubling atmospheric carbon dioxide on plant community development were examined by allowing seedling regeneration to occur from the natural seed banks present in samples of topsoil removed to laboratory microcosms from a productive tall herb community and an acidic grassland. Both communities were grown for about three months at 350 volumes per million (v.p.m.) and 700 v.p.m. CO_2 without nutrient addition. Further experimental details are provided in the legend to Fig. 1.

The doubling of CO_2 concentration did not produce a significant change in the total above-ground biomass in either of the two communities (Fig. 1). On the productive soil, the effect of elevated CO_2 on the two most common species, *Rumex obtusifolius* and *Cardamine flexuosa*, was to induce marked discolouration of the leaves and premature senescence of the foliage, which in the latter species coincided with a significant decline in yield. In both species these symptoms were associated with accumulation of non-structural carbohydrate, reductions in leaf nitrogen content and very large increases in soil microbial carbon and nitrogen (Fig. 1*a*).

No leaf symptoms were associated with the elevated CO_2 treatment applied to the acidic grassland community, although a large (but statistically non-significant) shift occurred in the relative abundance of the two most important species, with *Calluna vulgaris* expanding and *Agrostis capillaris* declining. In both of these plants, shifts in leaf carbohydrate and nitrogen concentrations were detected; these occurred in the same direction as those observed in the tall herb community but they were reduced in magnitude (Fig. 1*b*). Large increases in soil microbial carbon and nitrogen levels were again observed.

The induction of marked symptoms of nutrient deficiency in *Rumex obtusifolius* and *Cardamine flexuosa* by elevated CO_2 was surprising in view of the high productivity of the system from which the soil originated. The most likely explanation for this phenomenon is that increased carbon assimilation at enhanced

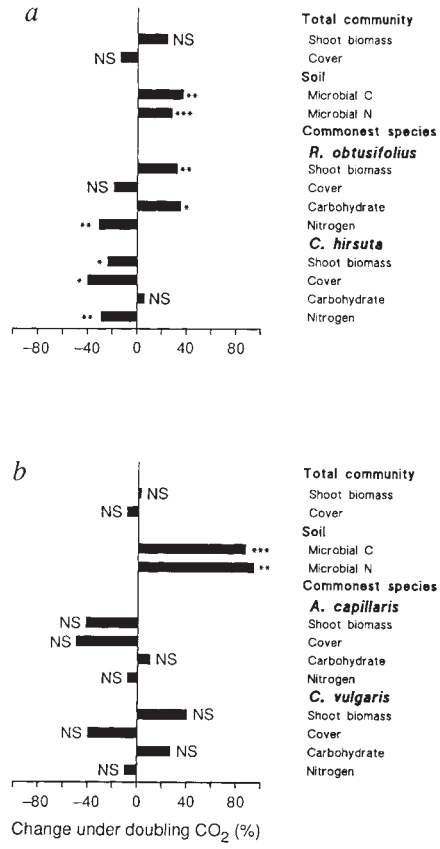

FIG. 1 Responses of commonest constituents and soil microflora grown in microcosms to a doubling of atmospheric CO_2 (700 v.p.m.) as compared with controls at 350 v.p.m. Topsoil samples with natural seed banks were collected from a tall herb community (*a*, Harpur Hill, Derbyshire, UK) and an acidic grassland (*b*, Ladybower, Derbyshire, UK) and placed in 2,400 ml microcosms (six replicates per combination of community type and CO_2 level). The microcosms were kept in 12 88,800-ml containers with individual control of CO_2 concentration and placed in growth cabinets. Vegetation was allowed to develop for 84 days (*a*) and 112 days (*b*) by natural recruitment from the seed banks, with periodic addition of deionized water. Growing conditions simulated those from early spring to late summer (12/12 h to 18/6 h light:dark, 16/10 °C to 25/16 °C light/dark; photosynthetic photon flux density was 240 ± 10 μmol cm^{-2} s^{-1}). Shoot biomass was measured as mg dry weight, cover as the number of touches in a point-quadrat analysis, carbohydrate[24] (starch + glucose + sucrose + fructan, when suitable) as mg g^{-1} fresh weight, and nitrogen[25] as mg g^{-1} dry weight of fully expanded young leaves, soil microbial biomass C[26,27] and N[27,28] as mg g^{-1} dry soil (fumigation techniques); NS, not significant; * $P \leqslant 0.05$; ** $P \leqslant 0.01$; *** $P \leqslant 0.001$ (ANOVA).